Microstructure and Water Adsorbability of Aircraft Combustor Soots and Kerosene Flame Soots: Toward an Aircraft-Generated Soot Laboratory Surrogate

O. B. Popovicheva and N. M. Persiantseva

Institute of Nuclear Physics, Moscow State University, 119992 Moscow, Russia

B. V. Kuznetsov, T. A. Rakhmanova, and N. K. Shonija

Chemical Department, Moscow State University, 119992 Moscow, Russia

J. Suzanne and D. Ferry

CRMC2-CNRS,† Campus de Luminy, case 913, 13288 Marseille Cedex 9, France

Received: February 17, 2003; In Final Form: September 9, 2003

The morphology, microstructure, surface area, porosity, and chemical composition of soot particles emitted from a gas-turbine combustor have been studied. Combustor soot particles appear to be chemically and structurally unstable and present microporosity and a strongly disordered graphitic structure. Discrepancies between the properties of combustor-generated soots arise from their postformation conditions, quenching environments, and sampling conditions. During long accumulation time, soot collected on the combustor walls experiences graphitization and oxidation. Upon long processing by hot exhaust gases, soot particles collected far from the combustor exit exhibit significant transformations (1) from paracrystalline to nodular amorphous microstructure and (2) from spherical particles to fused agglomerates following the increase in microporosity and oxygen content. Combustor-generated soot properties are compared to those of kerosene flame soot, which is produced in the laboratory and is proposed to be a surrogate of combustor soot for atmospheric studies. It is shown that the chemical composition, porosity, and extent of graphitization of combustor-generated and kerosene flame soots influence their electrical and hygroscopic properties. The characteristics of kerosene soot appear to be close to those of combustor soot but exhibit a number of specific feature variations such as graphitized nanostructure and ultramicroporosity, which influence its water adsorbability.

1. Introduction

Black carbon aerosols play a central role in global atmospheric phenomena such as cloud formation[1], radiative forcing,[2] and the chemical balance of the Earth's atmosphere.[3] The highest black carbon concentrations in upper troposphere can be found in regions over the U.S.A. and Europe, covarying in density with commercial air traffic fuel consumption.[4] Enhancement in the occurrence frequency of cirrus clouds up to 10% per decade[5] strongly suggests that emitted soot may act as ice nuclei for cirrus formation. Moreover, the reduction in the electrical conductivity of the troposphere with an increase of the soot particle concentration may be predictable because of the sensitivity of the atmospheric ion concentration to the aerosol abundance[6]. To quantify the effectiveness of aircraft-emitted soot particles to act as cloud condensation nuclei (CCN) and catalyze heterogeneous reactions, it is important to clarify their microphysical features and surface nature. Additionally, the electrical properties of carbon blacks varies widely depending on the crystalline form and chemical composition[7]. However, aircraft-generated soot particles are still poorly characterized. As a consequence, there is a considerable uncertainty regarding the quantitative estimate of the role of aircraft-generated soot aerosols in the atmosphere.

Most of the existing results concerning the hygroscopicity and heterogeneous reactivity of black carbon particles in the atmosphere are based on laboratory studies on spark discharge soot,[8−10] commercially available soots,[11−13] and laboratory-made hydrocarbon soots[14,15] with ill-determined soot surface properties. A laboratory combustion technique operating with a typical gas turbine engine combustor was used for soot sampling and its characterization in the recent work by Popovitcheva et al.[16,17] Combustor soot produced by burning a propane/butane mixture was collected close to the combustor exit. It was shown that the water adsorbability is considerably influenced by the soot surface heterogeneity and microporosity. However, the question of how the sampling procedure may impact the morphological and chemical properties of soots is still open. Indeed, recent studies[18,19] have shown that long residence times in the flame and exhaust gases induce postformation modifications of the soot microstructure. To evaluate the possible transformations of the soot particles during oxidation in the exhaust and hydration in the background atmosphere, comprehensive studies of the soot modified properties are required.

This paper is devoted to a study of the microstructure, texture, electrical conductivity, chemical composition, and water adsorbability of three kinds of aircraft combustor-generated soots collected both downstream of and inside the combustor. With

* To whom correspondence should be addressed. E-mail: suzanne@crmc2.univ-mrs.fr.

† Also associated with Université de la Mediterranée (Aix-Marseille 2) and Université Aix-Marseille 3.

10.1021/jp034402f CCC: $25.00 © 2003 American Chemical Society
Published on Web 10/31/2003

the underlying objective to identify a black carbon that can be used as a surrogate to study the aircraft-generated soot behavior in a laboratory-scale procedure, kerosene soot produced by burning aviation kerosene in an oil lamp was chosen for comparison. Four key parameters associated with black carbon morphology, namely, the size of primary particles, their internal microstructure, their surface area, and their porosity, are characterized by transmission electron microscopy (TEM) and gravimetry. Electron diffraction and Raman spectroscopy are used to determine the degree of graphitization. The electrical conductivity of sampled soots is correlated to their structural peculiarities. Soot elemental composition is examined by X-ray energy dispersive spectroscopy (XREDS) and atomic emission spectroscopy. A comparative analysis gives the specific features of each kind of soot related to its postformation processes and sampling conditions. This study highlights the water adsorption properties of soots and describes the specific behavior concerning their hydrophilicity treated within the framework of Dubinin's mechanism.[20]

2. Experimental Section

2.1. Soot Sampling. The combustion chamber of a gas-turbine engine has been used to produce the soot particles. As a first approach and because of the high cost of a kerosene compression station, we have used a fuel made out of gaseous propane/butane (9:1) mixture. The air/fuel ratio was ~4, which is close to cruise conditions. The schematic diagram of the combustor and the conditions of combustion have been described in detail in Popovicheva et al.[16] Three soot samples have been collected for this study. The first one was collected from the exhaust gas during a few combustion experiments. An air-cooled stainless steel probe was fixed to the exhaust pipe close to the combustor exit at a distance of 12 cm to minimize the time of contact with reactive exhaust gases. The exhaust temperature close to the probe was near 700 K. We will call this soot "combustor soot". The second sample, called "remote soot", was collected far from the combustor exit, at a distance of ~100 cm, after many repeated combustion experiments. The third soot sample, designated "inside soot", accumulated on the surface of the front device inside the combustion chamber and was brushed away from the walls after a long operation of the combustor. The collected soots were carefully stored in a glass bottle so that no foreign matter should inadvertently be added.

Additionally, we have chosen the simplest way to produce a laboratory-made soot, which may be used as a surrogate for atmospheric studies. Kerosene flame soot is produced by burning aviation-turbine kerosene fuel in a laboratory lamp burner. Soot is collected at a distance 15−20 cm above the flame on a glass support and stored under vacuum until laboratory examination. No other sampling procedure has been used. It is likely that other sampling conditions, closer to or further from the flame or with different fuel/air ratio, would exhibit different chemical and physical properties.

2.2. Physical Characterization. The size, bulk and surface microstructure of the primary particles and aggregates are analyzed by TEM (JEM 2000 FX JEOL (200 kV)) with a resolution of 2.8 Å. The soot particles are fixed on amorphous carbon microgrids. The shape of the crystallites in the soot particles is observed by the method of phase-contrast imaging, and the crystallite sizes are determined by electron diffraction and Raman spectroscopy.

The Raman spectrometer (B&M Spectronic BM-100) has a grating of 1200 lines per millimeter. Raman spectra are measured using the 5145 Å line of an 8 mW argon laser and the scattered radiations are collected in a "180°" configuration. Spectra are recorded in the 568−3900 cm^{-1} Stokes range with a resolution of 0.3 Å per channel and a time of accumulation near 4 s per channel. Band positions, as well as widths and intensities, are determined by curve fitting assuming Lorentzian band shapes. The Raman features in the spectral region from 500 to 2000 cm^{-1} can be related to the graphite-like microstructure of soots.

2.3. Chemical Composition. The TEM is coupled to XREDS for chemical composition analysis. The average chemical composition of soot is obtained after examination of five different areas to determine the carbon, oxygen, nitrogen, sulfur, and any metal content of soot. The sensitivity is near 0.3 wt %. Hydrogen content cannot be obtained by the XREDS technique. The elemental composition is also determined by atomic emission spectroscopy with a sensitivity of 10^{-3} wt %. The Raman spectra provide some bands characteristic of chemical bonds in the spectral region from 2000 to 4000 cm^{-1}.

2.4. Surface Area and Porosity Analysis. Gravimetric adsorption isotherm measurements of C_6H_6 at 298 K and N_2 at 77 K have been performed with a McBain scale and with an electromagnetic scale, respectively.[21] The sensitivity of the scales is 0.1 mg/g; the experimental accuracy is 1−3%. Prior to adsorption, the soot samples are heated to 473 K and outgassed at 10^{-3} Torr for 10−30 h to provide a surface clear of impurities and preadsorbed water. During the adsorption measurements, the equilibrium mass is read when the mass change ceases. It takes from 2 to 10 h to reach the thermodynamical equilibrium, depending on pressure. To examine the specific surface area and pore structure of soots the classical BET analysis[20,21] and theory of micropores filling[22] is used. Typical for such studies, N_2 and C_6H_6 are chosen as probes. The method of comparative analysis based on a reference graphitized carbon black is chosen to obtain the information about the extent of structural and energetic heterogeneities of the soot surface, as well as to estimate the surface area.[23]

In addition, for combustor and kerosene soots, the specific surface areas are determined by N_2 thermodesorption. Comparison of the integral intensities of the soot thermodesorption peak with those of a well-defined reference sample provides us with an estimate of the specific surface area. For kerosene soot, the Kr adsorption isotherm is measured using the standard volumetric technique.

2.5. Conductivity Analysis. To estimate the soot electrical properties**,** the specific conductivity is measured by compacting the soot powder in a compression setup like a "thumb screw" device described by Gregg and Pope[24]. The fluffy powder of a known weight is poured in a mould and compacted at low speed. The experimental method includes the simultaneous measurement of the conductivity and the volume of the compacted soot. The highest density reached in our experiments is 0.5 g/cm^3, which corresponds to an applied compacting pressure of 10^6 N/m^2. We should note that we never approached the bulk density of solid carbon, which is near 2 g/cm^3. The electrical conductivity is measured by a E7-12 LCR-meter using a 1 MHz signal with an amplitude of 1 V. Graphite powder is also measured for comparison. Experiments for each soot have been carried out in triplicate.

2.6. Water Adsorption Isotherms. We have performed a series of experimental water adsorption/desorption isotherms cycles on all soot samples. Prior to adsorption, the soot sample is thermally treated to remove preadsorbed water and impurities, which may be accumulated on the soot surface from ambient atmosphere. Soot is heated at 473 K and outgassed at 10^{-3} Torr

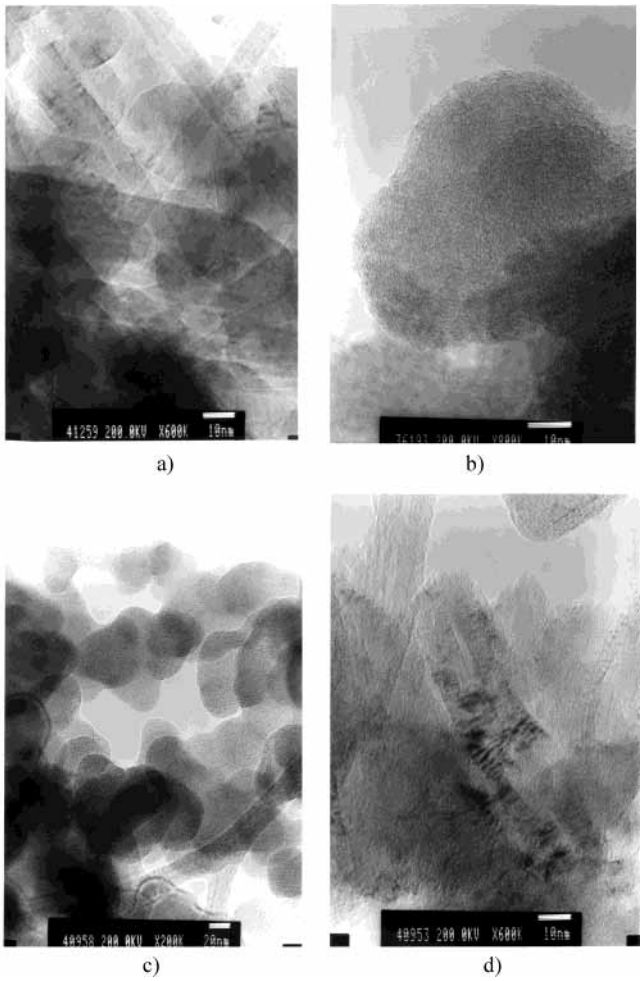

Figure 1. TEM phase-contrast image of soot particles for (a) kerosene soot, (b) combustor soot, (c) remote soot, and (d) inside soot (see text section 2.1 for soot definitions).

for approximately 30 h. The final criterion to end the heat treatment is an absence of desorption from soot surfaces during 30 min under vacuum.

3. Results and Discussion

3.1. Soot Morphology and Microstructure. The morphological features of soots have been examined by electron microscopy at 2×10^5, 6×10^5, and 8×10^5 magnifications and are shown in Figure 1 for kerosene, combustor, remote, and inside soots. Transmission micrographs indicate large aggregates composed of branched clusters of smaller coalesced particles. There is a remarkable similarity in the primary particle shape (roughly spherical particles) and diameters (between 30 and 50 nm) for all combustor-produced soots and for kerosene soot.

A comprehensive analysis of soots collected inside flames shows that the typical microstructure for a combustion-generated primary particle is amorphous or fullerenic carbon.[18] Appearance of ordered crystallite nanostructures such as onions and nanotubes requires long residence times that are available to the soot particles traversing the length of a flame. Therefore it is not surprising to observe some nanostructures in kerosene soot sampled above a flame. Figure 1a shows the heterogeneous mixture made of a few carbon nanotubes coexisting with amorphous-like spherical particles in kerosene soot. Nanotubes look like needlelike cylindrical tubes made of concentric graphite sheet multilayers with diameters of several nanometers and lengths up to 1 μm. The diffraction analysis shows clearly the crystalline nature of these particles.[25] The onion-like particles in kerosene soot are made of crystallites having a very small number of graphite planes, usually about 2 to 4, with a lateral extension of about 2−3 nm. These microcrystallites present a relaxed structure with interplane spacing larger than that in graphite. Micropores may formed between microcrystallites.

Roughly spherical particles of combustor soot collected close to the combustor exit exhibit a turbostratic onion structure made out of small graphitic crystallites oriented parallel to the surface, as seen in Figure 1b. The network of concentric graphite layers around several growth centers of rotation is called paracrystalline because it exhibits a degree of order somewhat between the true crystalline and the amorphous states.[26] The graphite layer planes show a wavy shape. This indicates that the atomic configuration of layer planes is far more random than that of graphite, involving numerous lattice defects and pores.

Surprisingly, an examination of the microstructure in remote soot collected far from the combustor exit does not show any nanostructures nor discrete spherical primary particles, as it can be seen in Figure 1c. A change to a totally amorphous nodular structure of aggregated fused individual particles seems to occur instead of the roughly onion-like spherical particles of combustor soot. It may be a result of the long contact of remote soot particles with hot oxidative exhaust gases as it was concluded by Clague et al.[19] for diesel exhaust soot. Oxidation of the combustor soot spherical particles may be followed by (1) the release of the volatile species such as the soluble organic fraction (SOF) or (2) crystallites stripping from the outermost shell,[27] which leads to the formation of fused agglomerates with a smooth surface without interparticle cavities, or both. As far as the internal microstructure is concerned, the long oxidation time leads to an atomic reconstruction and an increase of the amorphous state.

A quite different internal microstructure is observed for inside soot collected on the combustor walls. Figure 1d shows the nanotubes, which consist of about 20 concentric graphitic shells with conical caps. Such well-graphitized structures may be caused by high-temperature graphitization of the soot particles[16] accumulated on the combustor walls during long combustor operating time.

3.2. Degree of Graphitization. TEM data helps us to explain the main features of the Raman spectra for soots with varying degrees of disorder. For crystalline graphite a single line in the Raman spectra at 1575 cm^{-1}, which is commonly referred to as the G peak, is attributed to the C−C stretching vibrations. In the Raman spectra of all other graphitic materials, such as activated charcoal and various carbons, a second peak at 1355 cm^{-1} (D peak) is observed.[28] The D peak originates in aromatic skeletal vibrations, and its intensity increases (i) with an increase in the amount of "unorganized" carbon and (ii) with a decrease in the graphite crystal size. Figure 2 shows the experimental Raman spectra and their Lorentzian fits for combustor, remote, and kerosene soots. Such spectra are typical for amorphous carbon a-C in the microcrystalline graphite modification.[29] The existence of G and D peaks in the Raman spectra of all of our soots proves that the soot particles consist of small microcrystallites connected to each other by aromatic clusters and amorphous carbon.

The G and D peak positions are determined by several factors such as cluster sizes and their distribution, chemical content, and stress. The broadening of the G line is also strongly correlated to the size of the ordered two-dimensional regions in the graphite layers and to the chemical bonding. Table 1

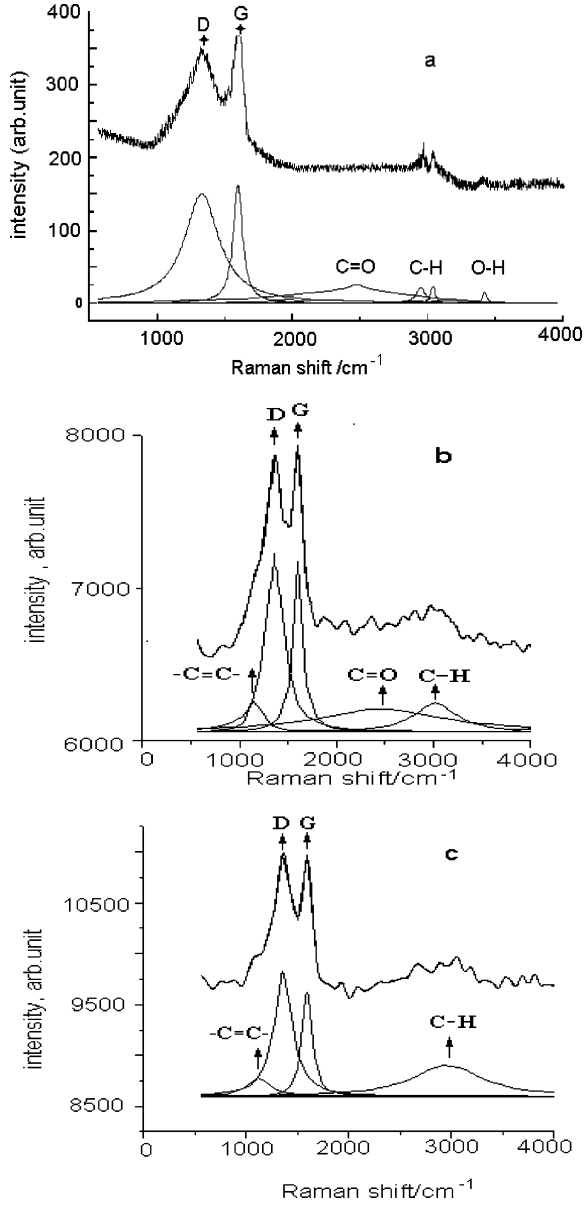

Figure 2. Raman spectra and Lorentzian fit for (a) combustor, (b) remote soot, and (c) kerosene soot. Top curves correspond to experiments and bottom curves to the fits.

TABLE 1: Raman Band Shape Parameters of Soots

sample soots	G band, cm^{-1}	D band, cm^{-1}	$\Delta\nu_G$, cm^{-1}	other peaks, cm^{-1} (band)
combustor	1595	1347	83	2500 (C═O), 2965 (C−H), 3041 (C−H), 3411 (O−H)
remote	1600	1363	116	1165 (C−C), 2458 (C═O), 3015 (C−H)
kerosene	1599	1364	99	1121 (C═C), 2961 (C−H)

presents the band shape parameters of Raman spectra for the various soots. One sees that the G position in remote soot (1600 cm^{-1}) is the farthest from that in crystalline graphite. Moreover, this soot reveals the highest broadening, $\Delta\nu_G = 116\ cm^{-1}$, in agreement with the TEM finding of the totally amorphous remote soot microstructure.

The measure of both the ratio of the peak intensities (I_D/I_G) and the G line width provides an indication of the degree of graphitization and allows a rough estimate of the cluster size.[29,30] The low ratio values $I_D/I_G \approx 1$ for our soots indicate their low degree of crystallinity and the presence of a small fraction of ordered aromatic rings. When the G line width increases beyond 50 cm^{-1}, the low ratio I_D/I_G indicates a cluster size smaller than 1 nm according to Schwan et al.[29] Many active sites for adsorption may be located on the edges of such small graphitic clusters made up of 5−6 fused aromatic rings. A disordered arrangement of the graphitic microcrystallites may lead to the formation of pores inside the soot particles.

We were not able to obtain good fits just by considering the G and D peaks for both the remote and kerosene soots, see Figure 2bc. Acceptable fits could only be reached by adding one extra peak at approximately 1165 and 1121 cm^{-1} for remote and kerosene soot, respectively. These bands may be assigned to the C−C and C═C stretching vibration modes of polyenes[31] connecting the graphite sheets in the microcrystallites.

TABLE 2: Elemental Composition of Soots (wt %)

sample soots	C	O	other elements
combustor	95	5	≤0.001
remote	85.2	12.7	
inside	86.8	13.4	Si 0.01; Mn,Mg 0.01; Fe 0.01; Cu 0.01; Ca 0.01
kerosene	92.2	7.7	Si 0.005; Mn,Mg 0.01; B 0.005

3.3. Chemical Composition. An important question about soots, besides their formation, morphology, and structure, is their chemical composition, including bulk and surface elements. Table 2 lists the elemental composition of a few representative examples obtained by XREDS including data from Auger electron spectroscopy (AES) for combustor soot[16]. Within the experimental sensitivity of XREDS and AES, no nitrogen, sulfur, nor any metal additives have been detected in combustor-generated soots.

We have found other elements such as Si, Mn, Mg, and B in kerosene soot probably originated from kerosene fuel impurities. It is important to mention that these elements were not present at weight more than 10^{-3}% in combustor soot originated from propane/butane fuel and collected on the combustor exit. However, Ca, Si, Mn, Mg, and metals such as Fe and Cu accumulate in inside soot, probably because of the prolonged contact with the surface of the front device at high combustion temperatures. Here we should mention that the formation of nanotubes observed in inside soot may be initiated by chemical vapor deposition stimulated by metal (Fe) catalysis[32].

We paid strong attention to the oxygen content in our soot samples owing to its major effect on the hygroscopic properties of the carbonaceous materials.[20,33,34] We have found an oxygen content in combustor soot near 5 wt %. Relatively weak bands are observed in its Raman spectra in the 2000−4000 cm^{-1} range, as shown in Figure 2a. The symmetric and antisymmetric vibrations of the C−H in the methyl groups are observed at 2965 and 3041 cm^{-1}. The small bands at 3411 and 2500 cm^{-1} are tentatively assigned to the ν(OH) and ν(CO) vibrations, respectively. But the intensities of these bands are small indicating that the surface of combustor soot presents weak chemical irregularities.

In remote and inside soots, the oxygen content reaches approximately 13 wt %, that is, 2.5 times more than that in combustor soot. For remote soot, it may be attributed to secondary oxygenated products on the surface resulting from heterogeneous reactions of the hot oxidative exhaust gases. Effective oxidation could lead to the large broadening of the G peak in the Raman spectrum and the prominent ν(CO) vibrations band at 2458 cm^{-1}, as seen in Table 1 and Figure 2b. But the ν(OH) band observed in the combustor soot spectrum has disappeared. It is likely that the OH groups have been consumed during the heterogeneous reactions with exhaust gases.

TABLE 3: Surface Area and Texture of Soots

sample soots	S_{N_2}, m^2/g	$S_{C_6H_6}$, m^2/g	S_γ, m^2/g	W_{mi}, cm^3/g[a]	x_{mi}, nm	E_{mi}, kJ/mol	W_{me}, cm^3/g	x_{me}, nm	E_{me}, kJ/mol
combustor	52 (TD)	40	70	1.6×10^{-2} (C_6H_6)	1.15	10.4	2×10^{-2}	3.6	3.4
remote	104		109	4.7×10^{-2} (N_2)	1.13	11.4	1.6×10^{-2}	3.8	3.3
inside	78	75	89	3×10^{-2} (C_6H_6)	1.65	7.23	2.2×10^{-2}	2.9	4.1
				3.2×10^{-2} (N_2)	1.13	10.6			
kerosene	64 (TD)	21	58	0.4×10^{-2} (C_6H_6)	0.52	22.5	1×10^{-2}	3.4	3.8

[a] In parentheses, the probe molecule that was used for texture analysis is indicated.

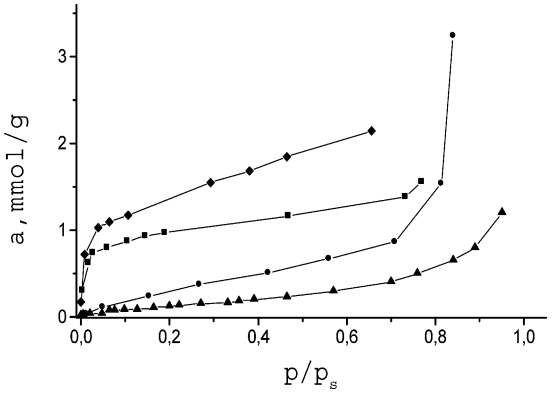

Figure 3. Isotherms of nitrogen adsorption ($T = 77$ K) on remote (♦) and inside (■) soot and of benzene adsorption ($T = 298$ K) on inside (●) and kerosene (▲) soot.

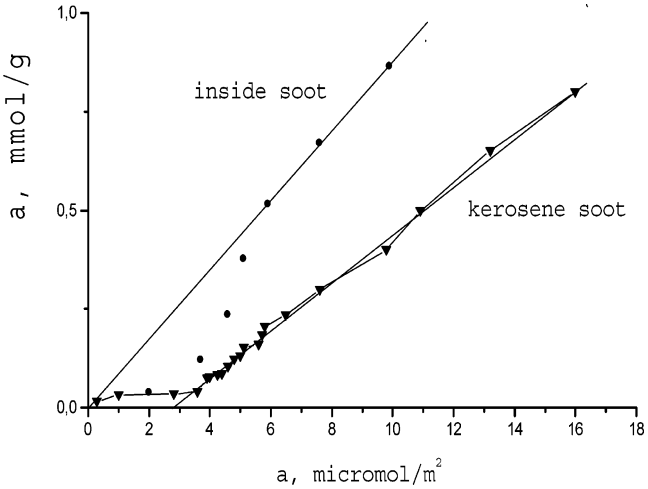

Figure 4. Comparative plots for benzene adsorption on kerosene (▼) and inside (●) soots using the adsorption data on graphitized soot.[35]

Kerosene soot exhibits near 7.7 wt % of oxygen as measured by XREDS, but it does not reveal any oxygenated features in the Raman spectrum such as ν(OH) observed with combustor soot or ν(CO) observed with remote soot. The most prominent bands are the vibrations of the C−H in the CH, CH_2, and CH_3 groups in the 2000−4000 cm^{-1} range.

3.4. Surface Nature and Area. Adsorption isotherms of N_2 and C_6H_6 are plotted in Figure 3. Table 3 presents the specific surface areas, S_{N_2} and $S_{C_6H_6}$, obtained using the adsorption data of N_2 and C_6H_6. For remote and inside soots, S_{N_2} is determined from the linear BET plot of the N_2 isotherm up to $p/p_S \cong 0.1$ (p_S is the saturation vapor pressure) assuming a N_2 molecular surface area w_{N_2} of 0.162 nm^2.[20] The C_6H_6 isotherm adsorption data are used to obtain $S_{C_6H_6}$ for combustor, inside, and kerosene soots in the initial range of relative pressures p/p_S up to 0.15 ($w_{C_6H_6} \cong 0.43$ nm^2). S_{N_2} (TD) is determined by the thermodesorption method (TD) for combustor and kerosene soot.

It is worth mentioning the difference in the values of the specific surface areas obtained with C_6H_6 and N_2 for combustor and kerosene soots: $S_{C_6H_6}$ is less than S_{N_2}. It may be attributed to the existence of micropores on the surface of these soots that are inaccessible to the large benzene molecule. From this assumption, the surface area determined for kerosene soot from Kr adsorption data, $S_{Kr} \cong 44$ m^2/g,[25] may be a more accurate value and will be taken below to determine the absolute adsorption isotherm of water.

Comparative methods are powerful tools to indicate the extent of structural and energetic homogeneities of the soot surfaces.[20] In our study, we use the comparative method, which is based on a comparative plot of the amount adsorbed in mol cm^{-2} for the reference sample against the amount adsorbed in mol g^{-1} for the sample under study.[23] The choice of a reference sample is a delicate question. It seems that thermally graphitized soot with a surface presenting structural and energetic homogeneities is the best choice among sootlike adsorbents. The generalized standard adsorption isotherms for C_6H_6 and N_2 on graphitized soots have been elaborated in Isirikian and Kiselev[35] and Voloshchuk et al.,[36] respectively, and used in our analysis. A linear comparative plot means high similarity of the adsorption isotherms for the studied soot and for the standard graphitized soot. Furthermore, the specific surface area, S_γ, can be determined from the slope of the plot. A concave comparative plot means a lower adsorption potential of the studied soot surface due to structural surface heterogeneities. Usually the concavity is observed in the monolayer region where the effect of the surface predominates.

The comparative plots for C_6H_6 adsorption on inside and kerosene soots are concave in the initial region up to $p/p_s \cong 0.5$, as shown in Figure 4, and therefore, they reveal a significant surface heterogeneity. At higher relative pressure, the impact of the surface nature become negligible and the linear plots allow an estimate of the soot surface areas. The values S_γ obtained for all soots of our study are presented in Table 3.

It is worth noting that the value obtained for S_γ is higher than that for $S_{C_6H_6}$ for all soot samples. A plausible explanation is that the C_6H_6 molecules increase the micropore size when they penetrate them, leading to an increase of the surface area. This so-called swelling phenomenon is also evidenced in irreversible adsorption and high hysteresis loops at low pressure. Swelling features were observed for all soot in our study and also in Popovitcheva et al.[16] for combustor soot and in Ferry et al.[25] for kerosene soot.

Special attention should be paid to the comparative plot of kerosene soot as shown in Figure 4. This plot is found to consist of two linear parts. The first one corresponds to the initial adsorption up to $p/p_s \cong 0.1$ and low S_γ calculated from the plot slope, which is characteristic of graphite. The slope of the second linear part provides us with $S_\gamma \cong 58$ m^2/g. This finding allows us to infer the existence of a mixture of two structural components in kerosene soot such as graphitized and amorphous soots. This hypothesis is also confirmed by our TEM observations and Raman spectra.

3.5. Adsorption and Porosity. To examine the pore structure of our soots, we have used the N_2 and C_6H_6 adsorption data.

The mechanism of adsorption is discussed in terms of the pore filling in Dubinin's theory[20]. The micropore volume and the average pore size may be determined by means of the fundamental Dubinin−Astakhov equation:[22]

$$a = \frac{W_0}{v^*} \exp(-(A/(\beta E_0))^n) \quad (1)$$

where a represents the amount adsorbed at the relative pressure p/p_S and the temperature T, W_0 is the limiting volume of adsorption or the volume of the micropores, v^* is the molar volume of the adsorbates, A is the change in Gibbs free energy upon adsorption, defined by

$$A = RT \ln(p_S/p) \quad (2)$$

E_0 is the characteristic energy of adsorption, and β is the affinity coefficient of the characteristic curves. Benzene is the reference molecule, and by definition, $\beta(C_6H_6) = 1$ and $v^* = 88.91$ cm^3/mol. For nitrogen, $\beta = 0.34$ and $v^* = 34.7$ cm^3/mol.[37]

Analysis of the linear representation of eq 1 for the adsorption of C_6H_6 on combustor, inside, and kerosene soots shows that the adsorption isotherms can be well approximated by a bimodal equation with $n = 2$ for a complex micropore structure:[22]

$$a = \frac{W_{01}}{v^*} \exp(-(A/(\beta E_{01}))^2) + \frac{W_{02}}{v^*} \exp(-(A/(\beta E_{02}))^2) \quad (3)$$

in which the parameters W_{01} and E_{01} and W_{02} and E_{02} correspond to two pore structures with different average sizes. For the N_2 adsorption data on inside soot, we found that $n = 3$ is more appropriate.

If one assumes a slit-shaped micropore model with a half-width x, there exists a relationship[22] between x and the characteristic energy E_0 in the form $x = k/E_0$ with a good approximation being

$$k = (13.028 - 1.53 \times 10^{-5} {E_0}^{3.5}) \text{ kJ nm/mol} \quad (4)$$

The specific behavior of C_6H_6, with a hysteresis extending to low pressures for all soots, indicates the slitlike nature of the micropores.[20] Therefore, we may use eq 4 for the determination of x_1 and x_2.

Here, we should note that the size of pores $x_2 \cong 2$ nm is situated on the classification boundary between the micropores and mesopores.[20] This is why we will define x_1 and x_2 as the sizes of micropores, x_{mi}, and mesopores, x_{me}. Table 3 gives x_{mi},W_{mi}, and E_{mi} and x_{me},W_{me}, and E_{me} obtained for combustor, inside, and kerosene soots using C_6H_6 adsorption data and for inside and remote soots using N_2 adsorption data. For all combustor-generated soots, x_{mi} is in the range 1.1−1.7 nm, but x_{me} is more than 3 nm. The most salient feature is the high micropore volume of remote soot, which is about 3 times larger than that of combustor soot. It is a great argument in favor of an oxidation process on the remote soot surface following the release of SOF species that creates the large microporosity. Moreover, remote soot presents the largest mesopore sizes, 3.8 nm, located between the fused agglomerates. It is surprising that only kerosene soot exhibits ultramicroporosity with $x \approx 0.52$ nm and a small micropore volume. It is reasonable to think that the low temperature in the lamp flame (∼1200−1400 K) does not allow a complete burning out of soot particles, which take places in the hot region of the engine combustor.

The total porosity, ϵ, of soot may be estimated from the density ρ of uncompacted beds of soots. This value was obtained roughly equal to 0.02 g/cm^3 for all soots of study. The total porosity of the bed is given by

$$\epsilon = 1 - \frac{\rho}{\rho_p}$$

where ρ_p is the primary particle density taken as 2 g/cm^3. Then the total porosity is 0.9. It represents overall bed and is a combination of micro- and mesoporosity of the particles and the void space in between.

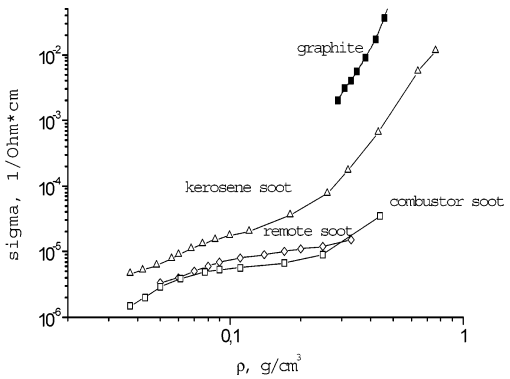

Figure 5. Electrical conductivity of compacts prepared from combustor (□), remote (◇), kerosene (△), and graphite powder (■) as a function of soot compact density.

3.6. Electrical Conduction. The electrical conductivity of any compacted powder is governed by three independent factors: (1) the conductivity of the primary crystallites of the material, (2) the conductivity across the interparticle contacts, and (3) the effect of the chemical inclusions.[7] It is useful to compare the soot conductivity with the value of a graphite powder, of which the conductivity properties are classified as semimetallic. Figure 5 shows the electrical conductivity, σ, of compacts of combustor, remote, kerosene, and graphite powders as a function of their density, ρ. The high value $\sigma \geq 2 \times 10^{-3}$ $(\Omega \cdot \text{cm})^{-1}$ for graphite powder reflects the high structural order in extended graphitic material. The conductivity of all soots is much less because the charge carriers are localized by the small dimensions of graphitic conductive islands (soot microcrystallites). Low conductivity of the onion-like amorphous particles of combustor and remote soots up to 0.2 g/cm^3 may be explained by charge tunneling between microcrystallites. Such a tendency is also characteristic of kerosene soot, but its higher conductivity may indicate the existence of a larger fraction of graphitic islands in agreement with our TEM findings.

The total area, and thus the conductivity, of the interparticle contacts is increased by compacting the powder under pressure. To describe the connectivity in random dispersed soots the theory of percolation has been used.[38,39] In a percolation process, charge carriers seek pathways offering minimum resistance. The steep rise in conductivity is observed above the percolation threshold at high level of compaction. For kerosene and combustor soot, as well as for graphite powder, a steep rise is observed above $\rho \cong 0.2$ g/cm^3, as shown in Figure 5, that is likely to be related to a percolation threshold.

Oxygen is an effective trap for charge carriers; it may affect the soot electrical conductivity. Indeed, remote soot with a high oxygen content has the lowest conductivity, whereas kerosene soot with the lower oxygen content has the larger σ. Additionally, to check the effect of oxygenated surface groups on the soot conductivity, the combustor soot sample was heated under vacuum at 573 K for 3 h. It results in an increase of σ by a factor 5 that we can relate to the release of the oxidized SOF species.

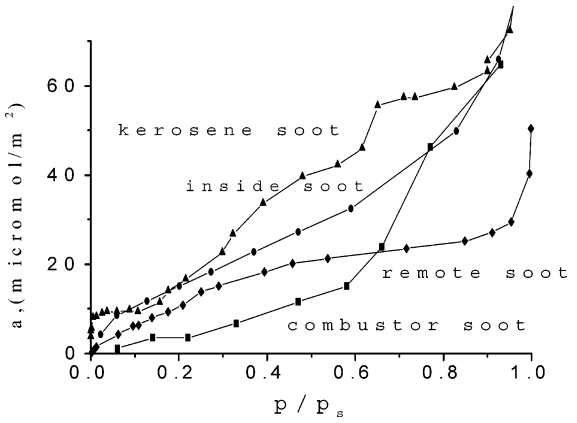

Figure 6. Water adsorption isotherms ($T = 295$ K) on combustor (■), remote (♦), inside (●), and kerosene (▲).

Soot particles may acquire some charge as a result of continuous charging and discharging events in a bipolar ion environment. The character of ion−soot interaction strongly depends on the electrical properties of the soot particles. Our soots feature conductivities that imply charge delocalization on the surface.[40] This means that the ion−soot interaction is dictated by both Coulomb and image forces. Hence, attachment coefficients should be increased when taking into account the image capture trapping.[41] Attachment coefficients of ions to kerosene soot particles were calculated in Popovicheva et al.[40] We can estimate to 5−45 h the characteristic time of the ion concentration reduction at the zonal mean perturbation of soot concentrations of ∼3−30 cm^{-3}.[39] As a consequence, that may result in a significant reduction of the electrical ionic conductivity in the atmosphere.

3.7. Water Adsorption. The peculiar nature of water adsorption on carbonaceous adsorbents is related to a relatively low dispersion energy between water molecules and graphite sheets. Within the framework of the Dubinin's theory,[34] water adsorption strongly depends on the presence of hydrophilic sites, so-called primary adsorption centers. According to the fundamental mechanism of water adsorption on carbonaceous adsorbents the initial water adsorption is likely to be due to oxygen-containing groups, which may act as primary adsorption sites. The graphitized soot, Graphon, possesses a well-defined hydrophobic and almost homogeneous nonporous surface with a very small fraction of hydrophilic heterogeneities, near 1/1500.[41] This is why the typical isotherm of water adsorption on hydrophobic Graphon is concave, and a small increase in adsorption is observed only at high relative pressures (type III of BDDT classification[20]) because of the secondary mechanism of adsorption on previously adsorbed water molecules (cluster formation).

The absolute adsorption isotherms at $T = 295$ K, calculated for unit surface on all of our soots are shown in Figure 6 for comparison. The values of S_{N_2}, presented in Table 3, for combustor-generated soots and S_{Kr} for kerosene soot were used. These adsorption isotherms cannot be referenced as type III because they exhibit a convex part at the lowest relative pressures, probably due to the existence of a significant amount of primary adsorption centers on the surface and also microporosity. If we assume that the amount of primary adsorption centers correlates with the oxygen-containing groups, we can explain the high water adsorption for remote and inside soots, which contain elemental oxygen ≅ 13 wt %. Moreover, the oxygen-containing groups were clearly determined by Raman spectroscopy. Kerosene soot presents the most prominent convex isotherm at the lowest p/p_S related to the relatively large adsorption potential in the ultramicropores (see Table 3). Probably, oxidized ultramicropores serve as primary adsorption sites in the case of kerosene soot.

TABLE 4: Water Adsorption Parameters

sample soots	a_m, mmol/g	S_{H_2O}, m^2/g	S_{H_2O}/S_{N_2}	χ_{mi}, %	χ_{me}, %
combustor	0.25	15	1/3.5	23	33.3
remote	122	72	1/1.4	48	20
inside	1.2	73	∼1	46	34
kerosene	0.36	22	1/2[a]	5.6	16.6

[a] S_{Kr} is used for kerosene soot.

The shape of the initial part of the water isotherms indicates the polar nature of the water-accessible surface. The comparative analysis of Figure 6 shows the high extent of polarity for all soot surfaces. If the amount of water adsorbed per unit surface of the hydrophobic reference material, graphitized soot Graphon, is used at $p/p_S = 0.2$, then inside and kerosene soots appear to be the most hydrophilic soots, approximately 750 times more hydrophilic than Graphon. Combustor soot is 200 times more hydrophilic than Graphon but less hydrophilic than inside and kerosene soot.

The amount of water corresponding to one water monolayer, a_m, may be determined by applying the BET theory to the water adsorption data in the range of low relative pressures up 0.1−0.2. Here it should be noted that in this case one water monolayer will correspond to roughly one water molecule adsorbed per active site. Moreover, it is obvious that this water monolayer is different from the statistical monolayer determined from adsorption isotherms of nonpolar molecules such as N_2 and C_6H_6. Then, the part of the surface area, S_{H_2O}, available for water is calculated assuming a cross-sectional area of water molecules of 0.1 nm^2.[20] The results are presented in Table 4.

To clarify the peculiarities of the water adsorption mechanism, it is possible to carry out a comparative analysis using the standard adsorption isotherm determined for the nonporous surface of a reference soot.[23] For this purpose, we plot the dimensionless adsorption ratio a/a_m for the material under consideration against the quantity $(a/a_m)_r$ determined for a reference sample, that is, graphitized soot Vulkan 7H[42]. The ratio a/a_m gives the amount of water molecules in a cluster formed on one primary center. The similarity of the water adsorption mechanism on the primary centers at low pressures for all soots reveals itself in the linear plot for the initial range of p/p_S. Deviation from a straight line indicates that the adsorption mechanism becomes different from independent cluster formation. It may happen at the confluence of water clusters when the distance between primary centers is less than the size of clusters formed during water adsorption. If the water adsorption takes place inside the micropores, a higher adsorption potential stimulates additional water adsorption and confluence of water clusters between the pore walls.[42,43]

Figure 7 presents the comparative plots for combustor, remote, and kerosene soots. The value of $a_m = 0.0065$ mmol/g for Vulkan 7H soot was obtained applying the BET theory. The resulting plot for all soots consists of two parts. The initially linear part for combustor soot up to $(a/a_m)_r \cong 4$ indicates the creation of independent water clusters from four water molecules near the primary adsorption sites. For relative pressures above $p/p_S \cong 0.6$, the experimental points deviate slightly upward, which indicates the confluence of the water cluster in the micropores.[42] Then they deviate downward from a straight line above $p/p_S = 0.8$. Here we should also note that the specific surface area of combustor soot S_{N_2} is approximately 4 times larger than the initial water accessible surface area S_{H_2O}, see

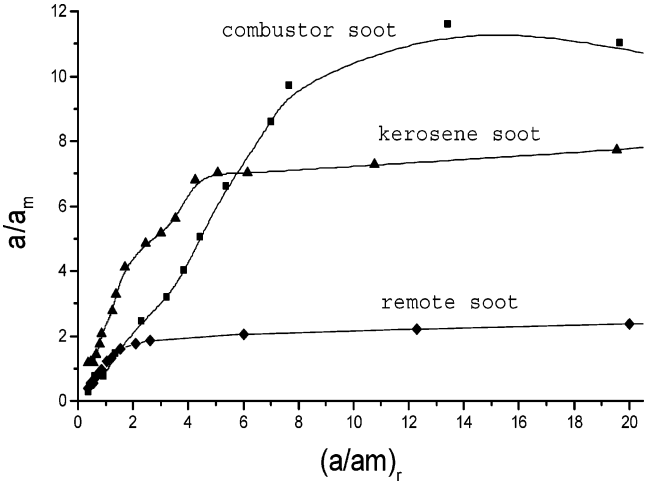

Figure 7. Comparative plot of water adsorption on combustor (■), kerosene (▲), and remote (♦) soots using the adsorption data on Vulkan 7H graphitized soot.[42]

Table 4; that is, 4 times more water molecules are needed to cover the whole soot surface. At relative pressures above $p/p_S \cong 0.6$, the steep rise in the adsorbed water amount was regarded in Popovitcheva et al.[16] as micropore filling due to capillary condensation. Again, from the deviation of a/a_m dependence above 4, we may conclude that the effective mechanism of adsorption in combustor soot above $p/p_S \cong 0.6$ is micropore filling, which should be followed by mesopore filling at $p/p_S \cong 0.8$.

For remote soot, the experimental points deviate downward from a straight line at $(a/a_m)_r \cong 2$ because of the large amount of primary centers, which indicates the appearance of a completely wetted surface already at $p/p_S \geq 0.53$. Let us note that the initially accessible surface area to water S_{H_2O} for remote soot is only 1.4 times less than that for nitrogen S_{N_2} (see Table 4). The effect of micropore filling is not as prominent as for combustor soot, as shown by the convex form of the isotherm already occurring at low pressures. The comparative plot for inside soot looks very similar to that for remote soot.

Moreover, it is generally accepted that the ratio of the surface areas determined for water and nitrogen adsorption can be utilized as a quantitative measure of the surface hydrophilicity. Ratios S_{H_2O}/S_{N_2} for the soots under investigation are also presented in Table 4. So, remote and inside soot appeared to be really oxidized soots because S_{H_2O}/S_{N_2} for them is close to 1. It is interesting to note that for spark discharge soot this ratio is only 1/10, which means a relatively hydrophobic surface with 10% of adsorption sites for water.[10]

Kerosene soot features the most complicated behavior with respect to water adsorption. For this soot, the comparative plot is not linear even at low relative pressures. As seen from Figure 7, for example, the value $(a/a_m)_r \cong 5$ on graphitized soot corresponds to $a/a_m \cong 7$ on kerosene soot. This means that at the same relative humidity approximately five water molecules are adsorbed per active center on graphitized soot, whereas seven water molecules are adsorbed per active center on kerosene soot. Increased adsorption on kerosene soot in comparison with adsorption on the separated centers on the homogeneous nonporous surface of graphitized soot indicates the possible confluence of water clusters originated on opposite walls of the ultramicropores in kerosene soot.

The specific features of water adsorption determine the wetting properties of soot. We should emphasize that monolayer water coverage, as well as micro- and mesopore filling, takes place for all soots of our study. Texture analysis allows us to estimate the amount of water that is needed to fill the volumes of micro- and mesopores of soots. Table 4 summarizes these finding. The fraction of water filling the pore volume is calculated as

$$\chi_{mi,me} = \left(\frac{W_{mi,me}\rho}{Ma_s}\right)100\%$$

where a_s is total amount of adsorbed water at $p/p_S \cong 1$, ρ is the water density, and M is the molar mass of water. For combustor soot, the amount of water filling the micropores is ~0.75 mmol/g, and that in mesopores is ~1.1 mmol/g which represents nearly 23% and 33.3% of the total amount of adsorbed water, respectively. Extra water may condense into water multilayers at higher $p/p_S \geq 0.95$ after capillary condensation in the mesopores.

Finally, we may conclude that the Dubinin's theory of micropore filling and mechanism of water adsorption allows us to describe the porous structure of all soot samples and the peculiarities of water adsorption on each of them.

4. Conclusion

Aircraft combustor soot produced by the gas turbine combustion technique is one of the best candidates to mimic the original aircraft-generated soot behavior in the atmosphere. The origin of the discrepancies between combustor-generated soots arises from the conditions of their postformation, quenching environments, and sampling conditions. It seems that the primary soot particles originate inside the combustor chamber of the gas turbine engine with an amorphous microstructure and some amount of oxygenated groups. Three kinds of combustor soots have been studied that follow quite different pathways: (i) In the case of combustor soot, it is collected and stored after the fast quenching on an air-cooled surface of the probe with little opportunity for chemical modification. (ii) For inside soot, which eventually accumulates on the front device inside the combustor chamber, long time contact with hot combustion gases and metallic surface allow oxidation, as well as nanotube growth, probably stimulated by metal (Fe) catalysis. (iii) Remote soot, collected far from the combustor exit, experiences relatively slower quenching in the gaseous oxidative environment of the exhaust system. For this latter soot, there are opportunities for physical and chemical changes. The transformation from paracrystalline to nodular amorphous structure and the formation of fused agglomerates occur after its formation. It seems that the combustor-generated soot particles have an unstable porous lattice structure, which may be easily modified under long exposure to hot oxidative gases because of the release of the soluble organic fractions or the stripping of outer layers or both. Moreover, the thermodynamic instability of the turbostratic structure allows heterogeneous reactions, which leave oxygenated secondary products on the remote soot surface.

We have compared the behaviors of these three kinds of combustor soots to that of kerosene soot obtained by burning aircraft kerosene in a laboratory wick lamp. Obviously, the laminar flow diffusion flame of the wick lamp differs appreciably from the highly turbulent combustion process in a modern gas turbine engine. Hence, one may question the relevancy of the present data in view of using the flame kerosene soot as an aircraft soot surrogate because it may give a distorted picture of an actual engine soot behavior. However, our comparative approach provides a unique way to understand the origin of the different behaviors. Kerosene soot is more similar

to combustor soot with respect to surface area and oxygen content, but it presents a graphitized nanostructure and an ultramicroporosity, which increase water adsorption at low relative humidities.

If the soot particles originate in the combustion region and are transferred by hot exhaust gases into the atmosphere, they would undergo exhaust oxidation, an increase of the surface area, of the porosity, and therefore of the hygroscopicity. But here we should note that prolonged oxidation processes affected the remote soot surface during many repeated combustion experiments in our investigation. Future studies that control the oxidation time and conditions are required.

The question to what extent the results of our laboratory studies can be transferred to scenarios of aircraft emission remains open because the data about the physicochemical properties of original aircraft-generated soot are scarce. We hope that the results presented in this paper will provide a useful basis for future studies, which are required to sufficiently quantify the physicochemical properties of atmospheric soot and their role in ice nucleation to form contrail and cirrus clouds.

Acknowledgment. The Russian scientists acknowledge the financial support of INTAS Programme through Grant No. 00-0460 and CRDF for Grant RC1-2327-M0-02. The authors gratefully thank Prof. A. M. Starik for fruitful discussions and cooperation in this work. Gratitude also is expressed to Prof. A. M. Starik's group of Central Institute of Aviation Motors of Moscow for soot production, to V. Pirogov for cooperation in the measurements of Raman spectra, and to Dr. R. Sh. Vartapetian for providing the experimental adsorption data on Vulkan 7H soot. S. Nitsche from CRMC2 (Marseille) is also gratefully acknowledged for his help in the TEM experiments.

References and Notes

(1) Sienfeld, J. H. *Nature* **1998**, *391*, 837.
(2) Buseck, P. R.; Postai, M. *Proc. Natl. Acad. Sci. U.S.A.* **1999**, *96*, 3372.
(3) Lary, D.; Shallcross, D. E.; Toumi, R. *J. Geophys. Res*. **1999**, *104*, 15929.
(4) Blake, D.; Kato, K. *J. Geophys. Res.* **1995**, *100*, 7195.
(5) Boucher, O. *Nature* **1999**, *397*, 30.
(6) Hoppel, W. A. In *Electrical Processes Atmospheres*; Dolezalek, H., Reiter, R., Eds.; Dietrich Stemkoff Verlag: Darmstadt, Germany, 1977; p 60.
(7) Spain, I. L. In *Chemistry and physics of carbon*; Walker, P. L., Ed.; Marcel Dekker: New York, 1981; Vol. 16, pp 119−259.
(8) Weingartner, E.; Burtscher, H.; Baltensperger, U. *Atmos. Environ*. **1997**, *31*, 2311.
(9) Kamm, S.; Möhler, O.; Naumann, K.-H.; Saathoff, H.; Schurath, U. *Atmos. Environ.* **1999**, *33*, 4651.
(10) Kuznetsov, B. V.; Rakhmanova, T. A.; Popovitcheva, O. B.; Shonia, N. K. *J. Aerosol Sci.*, in press.
(11) Lammel, G.; Novakov, T. *Atmos. Environ*. **1995**, *29*, 813.
(12) Rogalski, C. A.; Golden, D. M.; Williams, L. R. *Geophys. Res. Lett.* **1997**, *24*, 381.
(13) Choi, W.; Leu, M.-T. *J. Phys. Chem. A* **1998**, *102*, 7618.
(14) Longfellow, C. A.; Ravishankara, A. R.; Hanson, D. R. *J. Geophys. Res.* **2000**, *105* (D19), 24345.
(15) Gerecke, A.; Thielmann, A.; Gutzwiller, L.; Rossi, M. J. *Geophys. Res. Lett*. **1998**, *25*, 2453.
(16) Popovicheva, O. B.; Persiantseva, N. M.; Trukhin, M. E.; Shonija, N. K.; Starik, A. M.; Suzanne, J.; Ferry, D.; Demirdjian, B. *Phys. Chem. Chem. Phys.* **2000**, *2*, 4421.
(17) Popovitcheva, O. B.; Trukhin, M. E.; Persiantseva, N. M.; Shonija, N. K.. *Atmos. Environ.* **2001**, *35*, 1673.
(18) Grieco, W. J.; Howard, J. B.; Rainey, L. C.; Vander Sande, J. B. *Carbon* **2000**, *38*, 597.
(19) Clague, A. D. H.; Donnet, J. B.; Wang, T. K.; Peng, J. C. M. *Carbon* **1999**, *37*, 1553.
(20) Gregg, S. J.; Sing, K. S. W. *Adsorption, surface area and porosity*, 2nd ed.; Academic Press: New York, 1982.
(21) Brunauer, S. *Adsorption of gases and vapors*; Princeton University Press: Princeton, NJ, 1945; Vol. 1.
(22) Dubinin, M. M.; Stoeckli, H. F. *J. Colloid Interface Sci*. **1980**, *75*, 34.
(23) Karnaukhov, A. P.; Fenelov, V. B.; Gavrilov, V. Yu. *Pure Appl. Chem*. **1989**, *61*, 1913.
(24) Gregg, S. J.; Pope, M. I. *Fuel* **1960**, *39*, 301.
(25) Ferry, D.; Suzanne, J.; Nitsche, S.; Popovitcheva, O. B.; Shonija, N. K. *J. Geophys Res*. **2002**, *107*, 4734.
(26) Schirmer, A. In *Proceedings of Symposium on Emissions from continuos combustion systems*; September 27−28, 1971; Cornelius, W., Agnew, W. G., Eds.; Plenum Press: New York, 1972; pp 186−202.
(27) Ishiguro, T.; Suzuki, N.; Fujitani, Y.; Morimoto, H. *Combust. Flame* **1991**, *85*, 1.
(28) Tuinstra, F.; Koenig, J. *J. Chem. Phys*. **1970**, *53*, 1126.
(29) Schwan, J.; Ulrich, S.; Batori, V.; Ehrardt, H.; Silva, S. *J. Appl. Phys.* **1996**, *80*, 440.
(30) Knight, D. S.; White, W. B. *J. Mater. Res*. **1989**, *4*, 385.
(31) Dippel, B.; Jander, H.; Heintzenberg, J. *Phys. Chem. Chem. Phys*. **1999**, *1*, 4707.
(32) Yudasaka, M.; Kikuchi, R.; Ohki, Y.; Ota, E.; Yoshimura, S. *Appl. Phys. Lett*. **1997**, *70*, 1817.
(33) Kiselev, A. V.; Kovaleva, I. V. *Russ. J. Phys. Chem.* **1956**, *30*, 2775.
(34) Dubinin, M. M. *Carbon* **1980**, *18*, 355.
(35) Isirikian, A. A.; Kiselev, A. V. *J. Phys. Chem*. **1962**, *66*, 205.
(36) Voloshchuk, A. M.; Dubinin, M. M.; Moskovskaya, T. A.; Ivachnyuk, G. K.; Fedorov, N. F. *Bull. Acad. Sci. USSR, Div. Chem. Sci.* **1988**, *2*, 277.
(37) Dubinin, M. M. *Russ. J. Phys. Chem*. **1965**, *39*, 1305.
(38) Ehrburger-Dolle, F.; Lahaye. J. *Proc. II Int. Conf. Carbon Black* **1993**, 223.
(39) IPCC Special Report. *Avaition and the global atmosphere*; Penner, J. E., Lister, D. H., Griggs, D. J., Dokken, D. J., McFarland, M., Eds.; Cambridge University Press: Cambridge, U.K., 1999; p 69.
(40) Popovicheva, O. B.; Persiantseva, N. M.; Starik, A. M.; Loukhovitskaya, E. E. *J. Environ. Monit.*, in press.
(41) Young, G. J.; Chessick, J. J.; Healey, F. H.; Zettlemoyer, A. C. *J. Phys. Chem.* **1954**, *58*, 313.
(42) Vartapetian, R. Sh.; Voloshuchuk, A. M. *Russ. Chem. Rev*. **1995**, *64*, 985.
(43) Muller, E. A.; Rull, L. F.; Vega, L. F.; Gubbins, K. E. *J. Phys. Chem*. **1996**, *100*, 1189.